Constructing a Grain Boundary Sensitization-Embrittlement Map for Type 310S Stainless Steel Fuel Cladding in the Canadian SCWR Concept

Y. Jiao[1], Q. Wang[4], W. Zheng[2], D.A. Guzonas[3], M.R. Daymound[4] J.R. Kish[1]
[1]McMaster University, Hamilton, Ontario, Canada
[2] CanmetMATERIALS, Hamilton, Ontario, Canada
[3]Canadian Nuclear Laboratories, Chalk River, Ontario, Canada
[4]Queen's University, Kingston, Ontario, Canada
jiaoyn@mcmaster.ca, 13qw9@queensu.ca, Wenyue.Zheng@canada.ca, david.guzonas@cnl.ca, mark.daymond@queensu.ca, kishjr@mcmaster.ca

Abstract

The goal of this study is to identify the predominant grain boundary factor (sensitization versus embrittlement) that controls the intergranular stress corrosion cracking (IGSCC) susceptibility of austenitic stainless steel Type 310S exposed to supercritical water (SCW). Pre-treatments involving thermal ageing at high temperature in combination with plastic deformation were applied to induce specific types of grain boundary structure instability such as solute segregation, secondary phase precipitation and dislocation channeling. Each of these structural instabilities was independently assessed in terms of the susceptibility to both grain boundary sensitization and embrittlement in order to construct a 2-D property assessment grid Grain boundary sensitization was assessed using the double loop electrochemical potentiokinetic (DL-EPR) technique. Grain boundary embrittlement was assessed using nano-indentation and nano-scratching techniques. The susceptibility of the various degraded material will be evaluated using slow strain rate testing (SSRT) in 25 MPa SCW at 500 °C with 8 ppm dissolved oxygen in an autoclave flow loop (200 mL/min.) facility. This paper presents and discusses the results of our attempt to link the IGSCC susceptibility to a particular grain boundary degradation signature.

1. Introduction

The selection of a suitable corrosion-resistant fuel cladding material for the Canadian supercritical water-cooled reactor (SCWR) concept has received considerable attention [1,2]. The extreme nature of the predicted in-service environment includes a range of coolant temperatures, from subcritical (350°C) to supercritical temperatures (625°C), high pressure (25 MPa) and high dose of neutron irradiation (up to 9.5 dpa) [2]. From a corrosion resistance perspective, key attributes of the fuel cladding include an acceptable level of resistance to both corrosion/oxidation and stress corrosion cracking (SCC) damage.

Austenitic Fe-Cr-Ni alloys were identified as promising candidates early on in the development of the Canadian SCWR concept, and the results of a plethora of corrosion resistance assessments

conducted by the Generation IV International Forum partners support their continued consideration [1]. In large part, the corrosion resistance testing has been conducted using as-received (typically mill-annealed) material in as-machined condition, without much consideration of the microstructure instability that is expected to occur from simultaneous exposure to both high temperature and radiation during the in-service life (up to 30,000 h) of the fuel cladding [1,2]. While the effect of irradiation damage on the corrosion and SCC resistance has been given some consideration [3-5], the effect of thermal ageing damage has only been recently been recognized as a possible key factor affecting the corrosion resistance [6,7].

The SCC resistance of austenitic Fe-Cr-Ni alloys in SCW is influenced by its microstructure and metallurgical factors such as grain size, degree of cold work and irradiation damage [2-5, 8]. Grain boundary chemistry is also well known to affect the susceptibility to intergranular SCC as is the case with sensitized stainless steels [8]. In terms of microstructure instability, pre-exposure to high temperature irradiation has been found to significantly increase the intergranular SCC severity relative to the non-irradiated case, regardless of the irradiation dose or temperature [3-5]. In this case, the increased intergranular SCC severity correlated with both the contaminant increased hardening (introduced by either cold working or irradiation) and RIS (decreased grain boundary Cr content) [7]. This finding raises an important question about which factor, chemical (sensitization) or mechanical (embrittlement), controls the intergranular SCC mechanism operating in SCW.

The paper presents and discusses the current progress made in our attempt at using existing grain boundary sensitization and embrittlement characterization techniques to rank material pre-treated to induce a targeted instability in terms of increasing susceptibility to each. The goal is to construct a grain boundary sensitization-embrittlement property assessment grid that can be then linked to the intergranular SCC susceptibility as observed in SCW in order to identify the controlling factors.

2. Experiments

Rectangular test coupons (20 × 10 × 1 mm) were prepared from a commercial Type 310S austenitic stainless steel plate product provided in the mill-annealed (MA) condition. The chemical composition was shown in Table 1.

Table 1 Chemical composition (wt.%) of the Type 310S plate product.

Cr	Ni	Mo	Mn	Si	P	S	C	Fe
24.4	19.3	0.16	1.36	0.8	0.02	<0.001	0.06	Bal.

All microstructure instabilities considered herein were induced by thermal (heat) treatments only. A set of MA test coupons were solution annealed (SA) at 1050 °C for 1 h and water quenched to redissolve all of the problematic Cr-rich $M_{23}C_6$ precipitates that were present in the MA material. A subset of the SA test coupons were sensitized (S) at 650 °C for 100 h to form a network of Cr-rich $M_{23}C_6$ precipitates on the grain boundary that renders the material highly susceptible to

intergranular corrosion [9]. A second set of MA test coupons were sealed in an Ar gas purged quartz tube and thermally-treated (TT) for a 1000 h at 800 °C to precipitate the major intermetallic precipitates expected: $M_{23}C_6$ and sigma (σ) phase [10]. The temperature was selected to coincide with the maximum fuel cladding temperature expected in the Canadian SCWR design concept. Upon removal from the furnace, the test coupons were air cooled to room temperature while still sealed in the Ar-purged quartz tube.

The microstructure of SA, S and TT material was examined in cross-section using scanning electron microscopy (SEM), and transmission electron microscopy (TEM), both coupled with X-ray energy dispersive spectroscopy (EDS). The SEM examination was performed using a JEOL JSM-7000F microscope equipped with a Schottky Field Emission Gun (FEG) filament and an integrated Oxford Synergy system with INCA EDS micro-analysis using an accelerating voltage of 10 kV and a working distance of 10 mm. A single test coupon was cold-mounted in cross-section (with the section plane parallel to the long axis of the sample) and polished to a 1 μm finish. The TEM examination was performed using a JEOL 2010F TEM/STEM equipped with an Oxford Instruments EDS analyser using an accelerating voltage of 200 kV with a point-to-point resolution of 0.23 nm. The thin foil of each material required for TEM was prepared by mechanically-abrading an original rectangular sample to a thickness of 80 μm using SiC paper and water as the lubricant. A small section was then punched out of the mechanically-abraded sample and subsequently electrochemically polished in a perchlorate acid (10%)-methanol (90%) solution at -50 ºC to create a small hole.

The degree of sensitization of the SA, S and TT material was assessed using the double loop electrochemical potentiokinetic reactivation (DL-EPR) technique due to its sensitivity in capturing variations in the grain boundary Cr content [11]. DL-EPR tests were conducted in a three-electrode cell with a saturated calomel electrode (SCE) as the reference electrode. The test solution was 2 M H_2SO_4 + 0.01 M KSCN as suggested by Tavares et al. [9]. Working electrodes were prepared by attaching a Cu wire to the face opposite to the working surface face and then cold-mounting the coupon in an epoxy resin. The Cu wire was then inserted through a plastic tube that was sealed to the epoxy mount using more epoxy. The working surfaces were mechanically-abraded using 600 grit SiC paper and water as lubricant and then rinsed with ethanol. The working electrodes were immersed in the test solution for a period of 5 minutes to allow the open circuit potential to reach a steady state value. The applied potential was first swept in the forward (anodic) direction at a rate of 1 mV/s until the set point of +0.3 V_{SCE} was attained, after which it was swept in the reverse (cathodic) direction until the original open-circuit potential value was attained. The degree of sensitization is given as the current density ratio (i_r/i_a), where i_a is the activation current density peak observed in the anodic (forward) scan and i_r is the reactivation current density peak observed in the reverse scan. Triplicate measurements were made for each heat-treated material.

The degree of embrittlement of the SA, S and TT material was assessed as grain boundary hardness using both nano-indentation and nano-scratching techniques. A Digital Instruments Nanoscope platform was used for this purpose. The nano-indentation technique utilizes load-displacement data obtained during one complete loading and unloading cycle of the indenter [12]. The nano-scratching

technique utilizes a spherical indenter or an indenter with a spherical probe tip to plow through the material [12]. Coupon surfaces were polished to 0.05 μm finish using standard metallographic techniques. Nano-indentation measurements were made along parallel lines traversing grain boundaries in a given coupon with a 10 s dwelling time. A 60° included-angle conical diamond probe tip with a 1 μm spherical tip radius was used to make the nano-scratching measurements. Approximately 0.5 mN constant loading was kept to make a scratch across the grain boundary region. The hardness value determined from a nano-scratch is usually expressed as:

$$H = 8W/\pi w^2 \quad (1)$$

where W is the load (N) and w is the width (μm) of the scratch [12,13]. However, nano-scratching measurements were made in this case to quantify the degree of hardening of the grain boundaries exhibited by the SA, S and TT material. Hence, for this purpose, hardness was expressed as the scratch width (measured in both the austenite grain and grain boundary), and the degree of grain boundary hardening is expressed as:

$$R = w_g^2/w_{gb}^2 \quad (2)$$

where w_g is the average scratch width (μm) within the grain and w_{gb} is the scratch width (μm) within the grain boundary. The width of the scratch within the grain boundary was measured using the tapping mode of a Nanoscope III atomic force microscope (AFM). A set of 10 nano-indentation line scans were acquired across grain boundaries within each heat-treated material. A set of 6 nano-scratch line scans were acquired across grain boundaries in each heat-treated material.

3. Results and discussion

Table 2 summaries the microstructure instabilities observed on the grain boundaries of the SA, S and TT materials using TEM-EDS. Grain boundary Cr-rich $M_{23}C_6$ precipitates were still observed in the SA material. However, these remnant precipitates were widely spaced on the grain boundaries and there was no significant degree of sensitization (as measured by the width of the Cr-depleted zone) associated with them. In contrast, there was significant decoration of the grain boundaries by Cr-rich $M_{23}C_6$ precipitates observed in the S material, as well as a significant degree of sensitization. Significant decoration of the grain boundaries was also observed in the TT material. However, the dominant phase was σ rather than Cr-rich $M_{23}C_6$. Unlike the case for the S material and the Cr-$M_{23}C_6$ precipitates, there was no significant degree of sensitization associated with the grain boundary σ precipitates.

Table 2 Grain boundary instabilities observed by TEM-EDS.

Material	Dominant Precipitate	Degree of Decoration	Width of the Cr-dDepleted Zone (nm)
SA	Cr-Rich $M_{23}C_6$	Light	0
S	Cr-Rich $M_{23}C_6$	Heavy	200

TT	σ-phase	Heavy	0

Figure 2 compares the average i_r/i_a ratios for the SA, S and TT material, as determined from the DL-EPR measurements. The errors bars represent the 95% confidence interval. The overall ranking in terms of increasing i_r/i_a ratio (degree of sensitization in this case) is: SA < TT << S. The relatively low i_r/i_a ratio is consistent with the low degree of Cr-rich $M_{23}C_6$ precipitate decoration of the grain boundaries as observed by TEM. The relatively high i_r/i_a ratio of the S material is consistent with the heavy presence of Cr-rich $M_{23}C_6$ precipitate on the grain boundaries and associated measureable width of the Cr-depleted zone that neighbours the grain boundaries, as observed by TEM. The i_r/i_a ratio exhibited by the TT material was somewhat higher than that exhibited by the SA material, but still significantly lower than that exhibited by the TT material. The link between the i_r/i_a ratio and the grain boundary structure in this case was not straightforward and recorded a post-exposure examination of the polarized working surface.

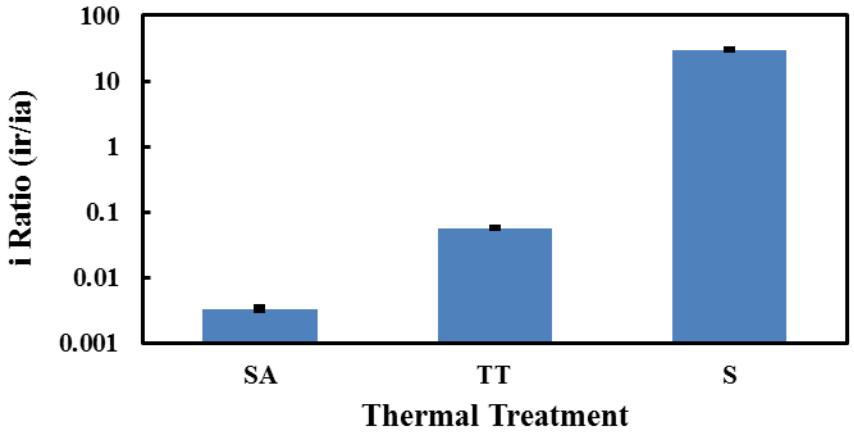

Figure 2. Degree of sensitization (i_r/i_a ratio) determined by DL-EPR testing.

Figure 3 shows a set of plan-view and cross-section view SEM images of the exposed SA, S and TT material, which document the mode and extent of corrosion that occurred during the DL-EPR test. The SA material showed very little grain boundary attack: slightly outlined in the plan-view image (Figure 3a) and no indications in the cross-section view (Figure 3b). The plan-view image of the S material (Figure 3c) exhibited significant grain boundary attack. Twin boundaries were also attacked, but to a much lower extent. Corrosion pits were observed to be uniformly distributed on the surface of the grains. The cross-section image (Figure 3d) revealed that the grain boundaries were attacked to a maximum depth of 10 μm. The widths of the attacked grain boundaries varied from the nanometre scale to the micrometre scale. Both the plan-view (Figure 3e) and cross-section (Figure 3f) image of the TT material revealed that the σ-phase was standing proud on the alloy surface, whereas the alloy matrix was preferentially dissolved. Thus, the i_r/i_a ratio of the TT material is a measure of the tendency of the matrix to preferential dissolve relative to the grain boundaries, which are heavily decorated with σ phase precipitates without an accompanying Cr-depleted zone.

a. SA (Plan-View)

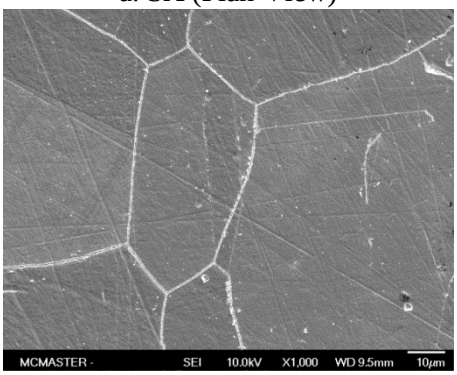

b. SA (Cross-Section)

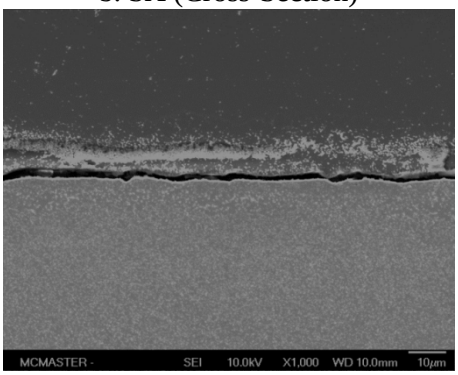

c. S (Plan-View)

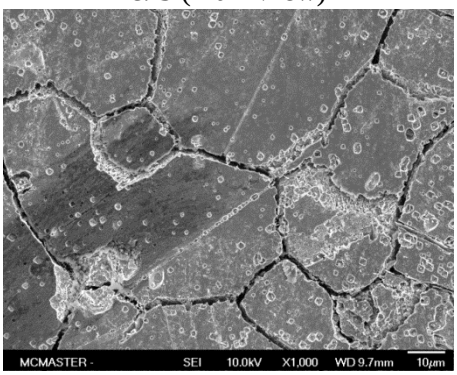

d. S (Cross-Section)

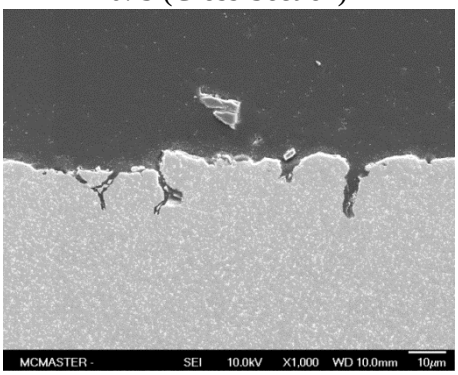

e. TT (Plan-View)

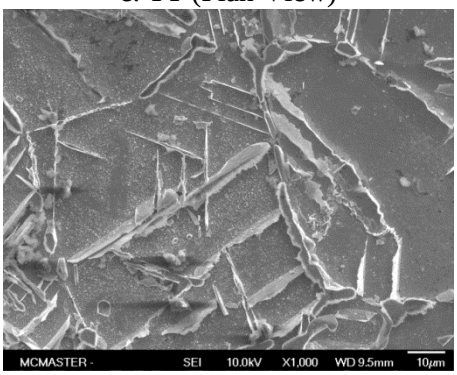

f. TT (Cross-Section)

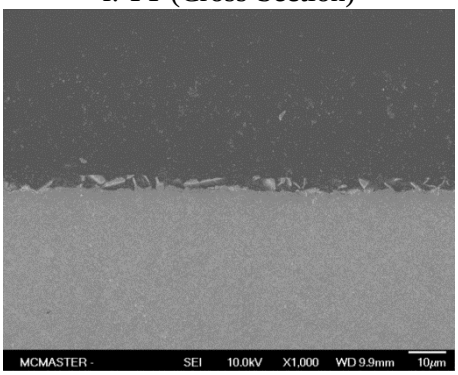

Figure 3 SEM images of the working surfaces of the SA, S and TT materials after DL-EPR testing.

The results of nano-indentation measurements are summarized in Table 3. The austenite grains of all three materials exhibited a similar average hardness value and the uncertainty represent the standard deviation. The nano-indentation hardness is highly sensitive to compositional variation [14] and indentation depth [12,14]. Formation of secondary phase precipitates within the austenite grains is well known to pin dislocations, which serves to increase the yield strength/hardness [15,16].

However, secondary phase precipitates can also consume solid solution strengthening alloying elements such as Cr, Mo, C and N [16]. It is possible that these competing factors have somewhat counterbalanced each other in the S and TT material, leading to a minor variation in the austenite grain hardness of each relative to the SA material.

Table 3 Nano-indentation hardness results.

Material	Grain-Boundary (GPa)	Grain (GPa)
SA	3.14 (±0.33)	2.45 (±0.20)
S	2.97 (±0.18)	2.60 (±0.23)
TT	6.35 (±1.75)	2.62 (±0.20)

In contrast, the hardness of the grain boundaries in the SA, S and TT material varied significantly. The overall ranking in terms of increasing grain boundary hardness is: S < SA << TT. The decoration of the grain boundaries by the Cr-$M_{23}C_6$ precipitates in the SA material likely accounted for the slight increase in hardness of the grain boundary relative to the matrix phase. The same likely holds true for the S material. The decrease in grain boundary hardness of the S material relative to the SA material despite the significant increase in the degree of precipitate decoration is likely related to the softening that occurs within the Cr-depleted zone. Such an effect has been reported in the literature [16]. Cr-rich $M_{23}C_6$ precipitates typically are of the nanometer scale in size and have a small volume fraction in austenitic stainless steels even after long-term ageing [17]. It is practically impossible to obtain the hardness of the Cr-rich $M_{23}C_6$ phase alone using the nano-indentation technique since the plastic deformation zone is about three times larger than the indents. Therefore, inclusion of the Cr-depleted zone in this measurement is unavoidable. The TT material exhibited the highest grain boundary hardness, as the hardness of the σ phase precipitates was likely measured in this case given their much larger size (1~2 μm in width and about 10~20 μm in length) relative to the Cr-rich $M_{23}C_6$ precipitates. The rather large uncertainty associated with this measurement is believed to be related to the variation in size of the σ phase precipitate measured, as it is likely that the plastic deformation zone may have extended into the austenitic matrix underneath a small-sized precipitate in some of the measurements.

A typical AFM image of the nano-scratching measurement in the SA, S and TT material is shown in Figure 4. The grain boundary in each image is contained within the superimposed white frame. Qualitatively speaking, the TT material exhibited the greatest relative change in the scratch width across the grain boundary region. Interestingly, slip bands were observed adjacent to scratch lines as a result of plastic deformation induced by the measurement in each material. The slip bands were observed to terminate at both the grain boundary themselves and at grain boundary precipitates.

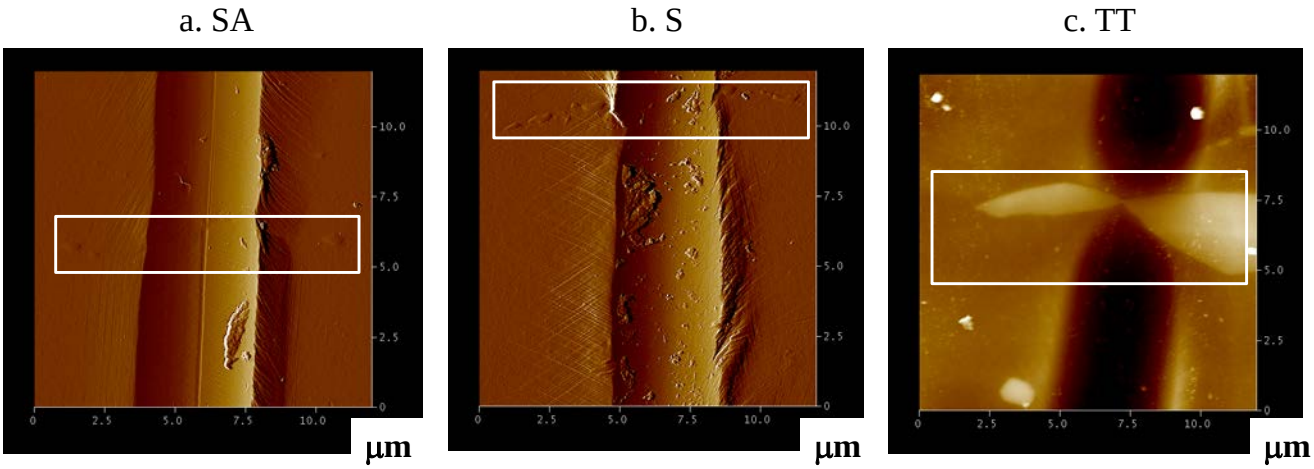

Figure 4 AFM images of scratch profiles across the grain boundary regions (framed).

The results of nano-scratching measurements are summarized in Table 4. The overall ranking in terms of increasing degree of grain boundary hardening (w_g^2/w_{gb}^2) is: SA < S << TT. The ranking is consistent with the σ phase precipitates showing high degree of decoration at the grain boundaries. The relative ranking of the grain boundary scratch width mirrored that of the overall ranking of the degree of the grain-boundary hardening. This was not the case for the set of grain scratch width measurements. Here the grains within the TT material were the softest of the three on average. This finding does not agree with the findings from the nano-indentation measurement, which suggested that the grains within the TT material were the hardest of the three on average. The simple explanation is that the secondary phase precipitates within the grains have consumed sufficient solid solution strengthening alloying elements such as Cr, Mo, C and N to create a local softening in the adjacent matrix. This would imply that these secondary phases were ineffective at pinning dissolutions. The root cause of this discrepancy is not well understood at this time and more work is required.

Table 4 Nano-scratching measurement results.

Material	With of scratch inside Grain (μm) (w_g)	Width of scratch across Grain Boundary (μm) (w_{gb})	Grain Boundary Hardening Ratio (w_g^2/w_{gb}^2)
SA	4.29 (± 0.26)	4.10 (± 0.26)	1.10
S	3.81 (± 0.26)	3.62 (± 0.26)	1.11
TT	4.97 (± 0.21)	3.36 (± 0.27)	2.23

Nano-indentation tends to provide a more accurate measure of the local hardness, whereas it may be difficult to capture the true hardness variation along a certain direction. Nano-scratching, on the other hand, is more suitable for hardness comparison as the locally hardened areas exhibit an observable decrease in the scratch width. However, the hardness suggested by nano-scratching is less accurate due to a hard secondary phase (such as σ phase precipitates) since they can be difficult to scratch under the same applied load, as shown to some extent in Figure 4c. A higher load would be likely required to leave a scratch on a hard secondary phase. However a higher load would likely decrease the resolution required to capture the scratch width variation [12]. Irradiation damage, which will need to be taken into account in the future, can lead to the formation of local hardened and softened areas [18], and the average hardness of the irradiated material could be three times larger than that of the unirradiated material [18] when the dose reaches a certain level. Considering this, the nano-indentation technique may prove to be a more meaningful technique for our purpose. A promising alternative to nano-indentation measurements may be micro-mechanical bending (load-displacement) measurements of grain boundary micro-cantilever beams prepared by focused ion beam (FIB) milling, as described in detail by Dugdale et al. [19]. The micro-cantilever beam measurements are capable of quantifying elastic moduli, yield stress (YS) and fracture toughness [19]. As FIB milling could ensure that applied stress and measured strain is concentrated on the grain boundary itself, this micro-cantilever beam measurement could give a more sensitive site-specific embrittlement metric.

Despite this, a grain sensitization-embrittlement map was created using grain boundary hardness as the embrittlement metric. The map is shown in Figure 5. The map is populated by the three heat-treated Type 310S materials under study: SA, S and TT. Superimposed onto the map are the boundaries that divide the space into four quadrants corresponding to the four distinct combinations of high and low sensitization and embrittlement. The boundary between high and low sensitization and embrittlement were arbitrarily set based on the relative rankings observed. Heat treatment alone as a means to induce microstructure instability in Type 310S was sufficient to populate three of the four sensitivity quadrants. An additional means of inducing microstructure instability is required to populate the fourth quadrant (high sensitization and high embrittlement). An attractive candidate is cold working. The intention is to cold-work both the S and SA material. Cold-working the S material is expected to populate the high sensitization and high embrittlement property space by creating dislocation sub-structures that can produce strain-localization at the grain boundaries, thus embrittling them [20]. Cold working the SA material is expected to do the same, but it (SA+CW material) will populate a space in the low sensitization and high embrittlement space at a lower sensitization level than that of the TT material. These postulations are being validated in the on-going work.

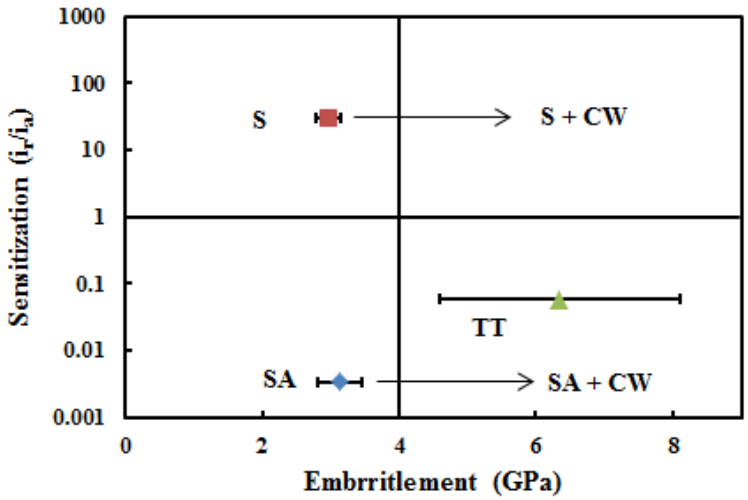

Figure 5 Concept of a grain boundary sensitization-embrittlement sensitivity map.

4. Conclusion

A grain boundary sensitization-embrittlement 2-D material property map, the first of its kind, is being constructed using existing grain boundary sensitization and embrittlement (hardness) characterization techniques to rank target microstructural instabilities intrinsic to Type 310S stainless steel. Once constructed, this property space will be linked to the intergranular SCC susceptibility as observed in SCW in order to identify the factors controlling this damage mechanism. The progress made thus far shows that the DL-EPR technique is an effective metric to rank the sensitivity to sensitization, which is considered to be the dominant chemical factor affecting the intergranular SCC mechanism. Both nano-hardness and nano-scratching measurements were considered as candidate metrics to rank the sensitivity to embrittlement, which is considered the dominant mechanical factor affecting the intergranular SCC mechanism. Both embrittlement characterization techniques had limitations, and a third technique based on load-displacement measurements of grain boundary cantilevers prepared by FIB milling is being assessed. The findings thus far also revealed that additional microstructural degredation treatments such as cold-working are expected to produce data to populate all four quadrants of the 2-D sensitivity map prior to SCC testing in SCW.

5. Acknowledgements

Funding to Canada Gen-IV National Program was provided by Natural Resources Canada through the Office of Energy Research and Development, Atomic Energy of Canada Limited, and Natural Sciences and Engineering Research Council of Canada. The expertise provided by Prof. Klassen's research group at Western University and the technical staff at the Canadian Centre for Electron

Microscopy at McMaster University is greatly appreciated for assisting with nano-indentation measurements and the microstructure characterization respectively.

References

[1] D. Guzonas, R. Novotny, “Supercritical water-cooled reactor materials – Summary of research and open issues”, Progress in Nuclear Energy, Vol. 77, 2014, pp. 361-372.

[2] W. Zheng, D. Guzonas, K.P. Boyle, J. Li, S. Xu, “Materials assessment for the Canadian SCWR core concept”, JOM, Vol. 68, 2016, pp. 456-462.

[3] S. Teysseyre, Z. Jiao, E. West, G. Was, “Effect of irradiation on stress corrosion cracking in supercritical water”, J Nucl Mater, Vol. 371, 2007, pp.107-117.

[4] R. Zhou, E.A. West, Z. Jiao, G.S. Was, “Irradiation-assisted stress corrosion cracking of austenitic alloys in supercritical water”, J Nucl Mater, Vol. 395, 2009, pp. 11-22.

[5] S.S. Raiman, A. Flick, O. Toader, P. Wang, N.A. Samad, Z. Jiao, G.S. Was, “A facility for studying irradiation accelerated corrosion in high temperature water”, J Nucl Mater, Vol. 451, 2014, pp. 40-47.

[6] J. Li, W. Zheng, S. Penttilä, P. Liu, O.T. Woo, D. Guzonas, “Microstructure stability of candidate stainless steels for Gen-IV SCWR fuel cladding application”, J Nucl Mater, Vol. 454, 2014, pp. 7-11.

[7] Y. Jiao, W. Zheng, D.A. Guzonas, W.G. Cook, J.R. Kish, “Effect of thermal treatment on the corrosion resistance of Type 316L stainless steel exposed in supercritical water”, J Nucl Mater, Vol. 464, 2015, pp. 356-364.

[8] Y. Watanabe, H. Abe, Y. Daigo, R. Fujisawa, M. Sakaihara, “Effect of physical property and chemistry of water on cracking of stainless steels in sub-critical and supercritical water”, in: Key engineering materials, Trans Tech Publ, 2004, pp. 1031-1036.

[9] S.S.M. Tavares, V. Moura, V.C. da Costa, M.L.R. Ferreira, J.M. Pardal, “Microstructural changes and corrosion resistance of AISI 310S steel exposed to 600-800C”, Materials Characterization, Vol. 60, 2009, pp. 573-578.

[10] W. White, I. Le May, “Metallographic observations on the formation and occurrence of ferrite, sigma phase, and carbides in austenitic stainless steels: Part I: Studies of AISI Type 310 Stainless Steel”, Metallography, Vol. 3, 1970, pp. 35-50.

[11] Y. Jiao, J. Kish, W. Zheng, D. Guzonas, "On the role of grain boundary chemistry in the intergranular stress corrosion cracking susceptibility of 310S exposed in supercritical water", in: The 7th International Symposium on Supercritical Water-Cooled Reactors, Proc. ISSCWR-7, Helsinki, Finland, 2015.

[12] N. Tayebi, A.A. Polycarpou, T.F. Conry, "Effects of substrate on determination of hardness of thin films by nanoscratch and nanoindentation techniques", Journal of Materials Research, Vol. 19, 2004, pp. 1791-1802.

[13] C.A. Brookes, P. Green, P.H. Harrison, B. Moxley, "Some observations on scratch and indentation hardness measurements", Journal of Physics D: Applied Physics, Vol. 5, 1972, pp. 1284-1293.

[14] M. Kunert, B. Baretzky, E. Mittemeijer, S. Baker, "Hardness-depth profiling on nanometer scale", Metallurgical and Materials Transactions A, Vol. 32, 2001, pp. 1201-1209.

[15] T. Sourmail, "Precipitation in creep resistant austenitic stainless steels", Materials Science and Technology, Vol. 17, 2001, pp. 1-14.

[16] P. Shankar, H. Shaikh, S. Sivakumar, S. Venugopal, D. Sundararaman, H.S. Khatak, "Effect of thermal aging on the room temperature tensile properties of AISI type 316LN stainless steel", J Nucl Mater, Vol. 264, 1999, pp. 29-34.

[17] T. Sourmail, H. Bhadeshia, "Modelling simultaneous precipitation reactions in austenitic stainless steels", Calphad, Vol. 27, 2003, pp. 169-175.

[18] P.M. Ahmedabadi, V. Kain, I. Samajdar, M. Gupta, S.C. Sharma, P. Bhagwat, Ajaykumar, "Effect of prior cold-work on radiation-induced segregation in proton-irradiated austenitic stainless steel", Corrosion Science, Vol. 60, 2012, pp. 153-164.

[19] H. Dugdale, D.E.J. Armstrong, E. Tarleton, S.G. Roberts, S. Lozano-Perez, "How oxidized grain boundaries fail", Acta Materialia, Vol. 61, 2013, pp. 4707-4713.

[20] Z. Jiao, J. Busby, R. Obata, G. Was, "Influence of localized deformation on irradiation-assisted stress corrosion cracking of proton-irradiated austenitic alloys", in: 12th International conference on environmental degradation of materials in Nuclear Power systems—water reactors, Salt Lake City, Utah, 2005.